



# Numerical investigation of non-linear inverse Compton scattering in double-layer targets

Marta Galbiati, Arianna Formenti, Mickael Grech, Matteo Passoni

## ► To cite this version:

Marta Galbiati, Arianna Formenti, Mickael Grech, Matteo Passoni. Numerical investigation of non-linear inverse Compton scattering in double-layer targets. *Frontiers in Physics*, 2023, 11, pp.1117543. 10.3389/fphy.2023.1117543 . hal-04310917

**HAL Id: hal-04310917**

**<https://hal.science/hal-04310917>**

Submitted on 28 Nov 2023

**HAL** is a multi-disciplinary open access archive for the deposit and dissemination of scientific research documents, whether they are published or not. The documents may come from teaching and research institutions in France or abroad, or from public or private research centers.

L'archive ouverte pluridisciplinaire **HAL**, est destinée au dépôt et à la diffusion de documents scientifiques de niveau recherche, publiés ou non, émanant des établissements d'enseignement et de recherche français ou étrangers, des laboratoires publics ou privés.



Distributed under a Creative Commons Attribution 4.0 International License

# Numerical investigation of non-linear inverse Compton scattering in double-layer targets

M. Galbiati, A. Formenti, M. Grech and M. Passoni

Department of Energy, Politecnico di Milano, Milano, Italy

E-mail: [marta.galbiati@polimi.it](mailto:marta.galbiati@polimi.it)

17 November 2022

**Abstract.** Non-linear inverse Compton scattering (NICS) occurring during the interaction of ultra-intense laser pulses with double-layer targets (DLTs) is studied with two-dimensional particle-in-cell simulations. The properties of this synchrotron-like photon emission are shown to be governed by the processes characterizing laser interaction with the near-critical and solid layers composing the DLT. In particular, electron acceleration, laser focusing in the low-density layer, and pulse reflection on the solid layer determine the radiated power, the emitted spectrum, and the angular properties of emitted photons. Analytical estimates, supported by simulations, show that quantum effects are relevant at laser intensities as small as  $\sim 10^{21}$  W/cm<sup>2</sup>. Target and laser parameters affect the NICS competition with bremsstrahlung and the conversion efficiency and average energy of emitted photons. Therefore, DLT properties could be exploited to tune and enhance photon emission in experiments and future applications.

*Keywords:* laser, plasma, non-linear inverse Compton scattering, particle-in-cell, simulation, double-layer target

## 1. Introduction

In the field of ultra-high intensity ( $> 10^{18}$  W/cm<sup>2</sup>) laser-plasma interactions, high-energy photon (x-rays and  $\gamma$ -rays) production has become of great interest for its impact on plasma dynamics (e.g. effects of radiation reaction on particles [1, 2, 3, 4]), for fundamental studies (e.g. investigation of quantum-electrodynamics (QED) in

strong fields [5] and plasmas [6, 7]), and for several potential applications. Some of these are plasma diagnostics [8], interrogation of nuclear materials [9], radiography [10], tomography [11], and imaging [12] for industrial and medical purposes, and photo-nuclear spectroscopy [13, 14].

Photon emission by electrons in laser-plasma interaction occurs mainly through two processes: bremsstrahlung mediated by high-Z atoms in dense-plasma regions [15, 16], and non-linear inverse Compton scattering (NICS) mediated by strong electromagnetic fields [5]. NICS is expected to be the dominant emission process at very high intensities when  $a_0 = eE_0/(m_e\omega_0c) > 100$ -200, where  $a_0$  is the normalized vector potential defined with the electron charge  $e$ , the electric field peak amplitude  $E_0$ , the electron mass  $m_e$ , the laser frequency  $\omega_0$ , and the speed of light  $c$ . Instead, bremsstrahlung strongly depends on the target atomic number  $Z$ , density and geometry. Thus, it is expected to dominate for thick enough, high-Z-material targets [17].

NICS is the process in which an electron absorbing multiple laser photons emits high-energy photons [5]. It is the quantum version of synchrotron emission important in the regime in which the ultra-high intensities of the electromagnetic fields and the high energy of the electron make relevant the spin effects, and the discrete view and stochasticity of the emitted radiation [3, 4]. The main parameter to describe this emission is a Lorentz invariant, usually referred to as the electron quantum parameter:

$$\chi = \frac{\gamma}{E_s} \sqrt{(\mathbf{E} + \mathbf{v} \times \mathbf{B})^2 - \left(\frac{\mathbf{E} \cdot \mathbf{v}}{c}\right)^2} \quad (1)$$

where  $\gamma$  is the emitting electron Lorentz factor,  $E_s = m_e^2 c^3 / (\hbar e) = 1.3 \cdot 10^{18}$  V/m the Schwinger field with  $\hbar$  the reduced Planck constant,  $\mathbf{v}$  the electron velocity, and  $\mathbf{E}$  and  $\mathbf{B}$  the electromagnetic fields at the electron position.  $\chi$  is related to the transverse acceleration exerted instantaneously by the electromagnetic field on the electron and determines the emission rate and the radiated power by the electron.  $\chi \rightarrow 0$  is the classical case of continuous emission in which the instantaneous photon emitted power is given by Larmor formula  $P_{rad} = 2m_e c^2 \alpha^2 \chi^2 / (3\tau_e)$  with  $\tau_e = e^2 / (4\pi\epsilon_0 m_e c^3)$  the time for light to cross the classical radius of the electron. For  $\chi \sim 1$ , the quantum effects become important. In particular, a single emitted photon carries a significant fraction of the electron energy, and the classical emitted power is corrected by a factor  $g(\chi)$  (see equation 4 in section 3) that reduces the radiated power, albeit

letting it always increase with  $\chi$ . From definition 1, it is easy to deduce that  $\chi$  peaks when the electromagnetic field propagation direction  $\mathbf{k}$  and the electron velocity  $\mathbf{v}$  are anti-parallel. In this condition,  $\chi \approx 2\gamma E_{\perp}/E_s$  [18], where  $E_{\perp}$  is the electric field perpendicular to the electron motion. In general, the emission is enhanced by this condition of counter-propagation and the combination of energetic electrons ( $\gamma \gg 1$ ) and intense fields ( $a_0 \gg 1$ ).

The first experiments on NICS have been performed by colliding a high-intensity laser pulse with a relativistic electron beam from a conventional linear accelerator [19]. In all-optical setups, NICS has been observed in several cases exploiting laser wakefield acceleration (LWFA) with either two counter-propagating laser beams [1, 2] or only one laser beam reflected from a plasma mirror [20]. However, the low density of the gas target in these schemes and, consequently, the limited number of high-energy electrons (bunch charge around tens of pC) keeps low the conversion efficiency from laser to photons [21, 22]. Higher efficiencies would be possible at higher densities in solid foils [6] or, even better, in near-critical targets [23], i.e. targets approaching the critical density  $n_c = m_e \omega_0^2 \epsilon_0 / e^2$  ( $\epsilon_0$  is the vacuum permittivity) and granting efficient laser-plasma coupling. Nevertheless, simple solid or near-critical slabs cannot easily ensure both efficient electron generation and the condition of laser propagating against electrons. Therefore, these cases have not yet been studied thoroughly in experiments, and numerical studies have revealed that they would require extreme intensities ( $> 10^{22}$ - $10^{23}$  W/cm<sup>2</sup>) to make the process efficient (conversion from laser to photons  $\geq 5\%$ ) [24, 25, 26, 27, 28, 29, 30, 31, 32].

A highly-developed target concept, like a double-layer target (DLT), could allow exploiting NICS more efficiently than the LWFA case and performing more accessible studies for current laser facilities. The DLT we consider here consists of a low-density layer placed on a solid substrate. The low-density layer is near-critical at laser wavelength around 1  $\mu\text{m}$  and can be obtained by growing a nanostructured material (*foam*) on the substrate [33, 34, 35]. Laser propagating against electrons is achieved in DLTs thanks to the substrate acting as a plasma mirror like in [20]. At the same time, the near-critical layer enhances the hot-electron generation producing a high-charge (tens of nC) population of energetic electrons during the interaction [36]. In practice, the substrate reflects the laser pulse creating an overlap between the reflected field and the hot electrons efficiently accelerated before reflection by the laser itself. The fulfilment of the counter-propagation condition makes the DLT a promising scheme for NICS, as proved by some numerical studies

[37, 38, 39, 40, 41, 42] and investigated by some of us as supervisors of [43]. Consequently, as demonstrated in [44], DLTs could become interesting for electron-positron pair generation at extreme intensities ( $\sim 10^{23}$  W/cm<sup>2</sup>). At the same time, by choosing a micrometric DLT with low-Z layers, we can focus on NICS also in non-extreme regimes of laser-plasma interaction ( $a_0 \sim 20-60$ ) since bremsstrahlung production yield has proven to be low in this case [45, 46].

The micrometric target case and the time scales of NICS, which follow the typical laser pulse time scales of tens of fs, are accessible to particle-in-cell (PIC) simulations. PIC codes, well-established tools to simulate collisionless plasmas in self-consistent electromagnetic fields, have been recently enriched with several packages to simulate additional physics, including synchrotron-like emission. One of the most feasible and accurate ways to simulate photon emission via NICS inside PIC codes is a Monte Carlo method [47]. This strategy adopts a semi-classical approach using emission rates calculated in the locally constant crossed field approximation (LCFA), which assumes only first-order QED processes and is now standard in many PIC codes [48, 49, 50].

An in-depth numerical investigation of NICS during laser-DLT interaction is preparatory to any experimental campaign. Even if some numerical studies of NICS in DLTs or similar regimes exist, most of them focus on the very high-intensity regime,  $a_0 \sim 100-300$ , which is not ordinary in current laser facilities and was only recently achieved experimentally [51]. For these reasons, in this work, we study NICS in DLTs at non-extreme intensities ( $a_0 \sim 20-60$ ) with a sizeable numerical scan of 2D PIC simulations performed with Smilei [52], a PIC code capable of simulating NICS. We focus first on the physical aspects of interaction and emission. Second, we reconstruct some emission properties analytically to test the numerical tool and evaluate the impact of quantum effects in this regime. Then, we compare NICS and bremsstrahlung in some selected cases to estimate the possible competition between the two processes in an experimental framework. Finally, we analyse the emission properties considering all the laser intensities and target parameters (foam density and length) studied in the simulation scan.

## 2. Methods

We have investigated NICS in DLTs with the PIC code Smilei. This code embarks a Monte-Carlo module for NICS based on the approach presented in [49]. This

approach relies on the emission rates obtained with LCFA (see discussion in [3]) and allows treating high-energy photons as macro-photons. When emitted, these macro-photons are created with a momentum pointing in the direction of the emitting electron, an approximation valid in the relativistic limit [53].

We have performed 2D simulations of a laser pulse interacting with a DLT. The simulation resolution is 62.5 points per  $\mu\text{m}$  in a box of 40.96  $\mu\text{m}$  in  $y$  and variable in  $x$  from 34 to 74  $\mu\text{m}$  according to the target length. The simulation duration changes too according to the target length from 138 fs to 272 fs. The laser pulse peak enters the simulation box from the  $x = 0$  boundary nearly 20 fs after the beginning of the simulation. The laser pulse has wavelength  $\lambda=0.8 \mu\text{m}$ , a  $\sin^2$  temporal profile in intensity with FWHM=20 fs and a Gaussian spatial profile with a waist (radius at which the field amplitudes fall to  $1/e$ ) of 3  $\mu\text{m}$ , corresponding approximately to an  $f/4$  focusing aperture. The laser is linearly polarized in the  $y$  plane of the box. These laser parameters have been chosen to be characteristic of forthcoming experiments on multi-petawatt, ultrashort, Ti:Sapphire laser systems as Apollon [54]. The target is a DLT with a fully-ionized homogeneous carbon ( $Z=6$ ,  $A=12$ ) foam on top of a fully-ionized aluminium ( $Z=13$ ,  $A=27$ ) layer of 2  $\mu\text{m}$ -thickness and density  $450 n_c$ . The choice of fully-ionized target layers results from having tested, considering field ionization in additional simulations, that the target atoms involved in the interaction rapidly get fully ionized at  $a_0 \geq 20$ . The foam electrons are represented with up to 10 particles per cell (ppc) according to the layer density, foam ions with 1 ppc, substrate electrons with 32 ppc, and substrate ions with 3 ppc. Electrons are initialized with a temperature of 10 eV, and ions are initialized cold. Photon generation via NICS is switched on only for photon energy above  $0.25 mc^2$  and for  $\chi > 10^{-4}$ . NICS is simulated with the default tables of Smilei, and pair production is neglected. We have performed 80 simulations exploring all the combinations of the following parameters: foam density  $n_e=1, 2, 5, 10 n_c$ , foam thickness=5, 10, 15, 20, 25  $\mu\text{m}$ , and intensity  $I=0.87, 3.46, 5.41, 7.79 \cdot 10^{21} \text{ W/cm}^2$  ( $a_0=20, 40, 50, 60$ ). A special simulation, called simulation A, characterized by  $a_0=50$ , foam thickness = 15  $\mu\text{m}$  and foam density= $2 n_c$  was performed with a high temporal resolution of the diagnostics. We will use it in section 3 to describe the physics of the interaction and the main properties of NICS in DLTs.

### 3. Results and discussion

### 3.1. Description of interaction and emission

We start reporting the results of simulation A (see section 2). We use this simulation to describe the main aspects of the laser-DLT interaction and the consequent NICS emission. Figure 1 helps to visualize the behaviour of the laser and hot electrons during the simulation.

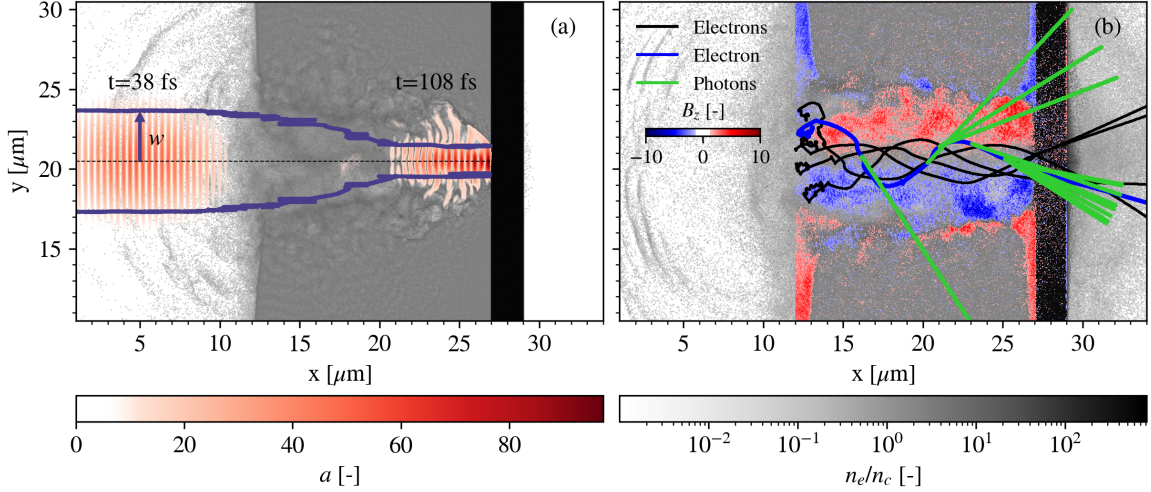


**Figure 1.** Evolution of the laser and trajectories of some electrons in simulation A. Plot (a) shows in blue lines the laser waist limits, calculated as the points where the field amplitude falls to  $1/e$  of its maximum, and two snapshots of  $a = e|\mathbf{E}|/(m_e\omega_0c)$  at 38 fs and 108 fs. The black dashed line indicates the centre of the box in  $y$ . Plot (b) shows some trajectories of electrons and photons and the field  $B_z$  normalized to the code units at 204 fs. The represented electrons (black and blue lines) are characterized by a final value of kinetic energy above 60 MeV. The photons (green lines) are emitted by the electron represented in blue. In the background of both plots, the electron density normalized to  $n_c$  at 108 fs in (a) and 204 fs in (b).

Before the interaction, the laser pulse focused on the target left boundary undergoes free-propagation (Figure 1 (a) laser snapshot at 38 fs). When the interaction with the low-density layer starts, the pulse experiences a progressive alteration of its spatial and temporal shape, and a gradual absorption [55]. The near-critical plasma behaves as a lens causing relativistic self-focusing [56, 57, 58]. This phenomenon induces the reduction of the laser spot size, the increase of the laser pulse intensity, and, consequently, the pulse confinement in a channel in which the electron density is depleted because of the ponderomotive force. As shown by the blue line in

Figure 1 (a), the laser waist is decreased symmetrically inside the foam from 3  $\mu\text{m}$  down to nearly 1  $\mu\text{m}$ . During the interaction with the near-critical layer,  $a_0$  increases from 50 to 70 and goes above 100 when the laser is reflected on the substrate (Figure 1 (a) laser snapshot at 108 fs). As a consequence of reflection, the laser intensity is further enhanced due to the superposition of the incident and reflected pulse. A temporary standing wave builds in front of the substrate, and the peaks of the normalized electric field  $e|\mathbf{E}|/(m_e\omega_0c)$  and magnetic field  $e|\mathbf{B}|/(m_e\omega_0)$  alternatively grow up to 150 at the nodes and antinodes of this wave. Since self-focusing and superposition can generate a much shorter and stronger laser pulse with higher peak intensity, these processes are important to boost NICS. Another phenomenon is the magnetization of the channel [59]: following the laser pulse propagation, the  $B_z$  component of the field fills the channel in two symmetric regions of opposite signs (Figure 1 (b)).

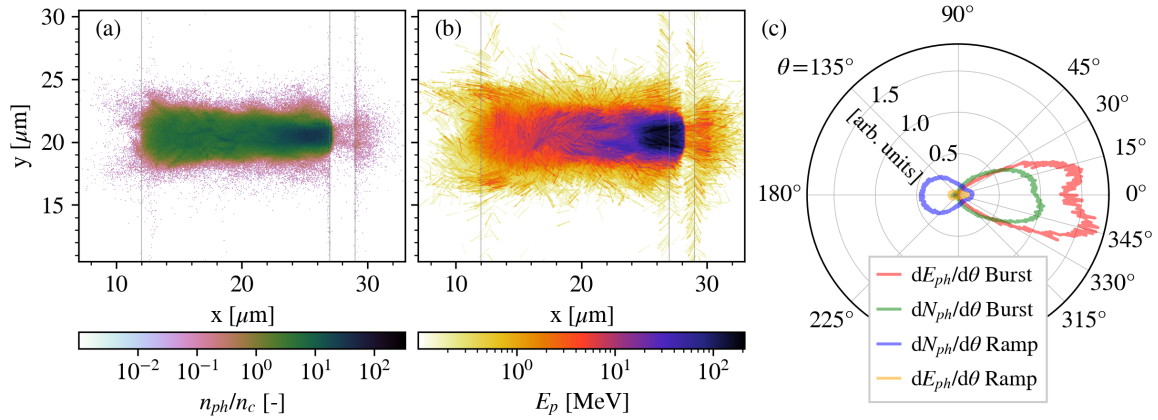


**Figure 2.** Spatial and angular information on photon emission: the distribution in space of photon number density normalized to  $n_c$  (a), the emitted photons represented as arrows directed according to their momentum and coloured according to their energy  $E_p$ , and the photon angular distribution in number and energy (c) for the two phases of emission, i.e. ramp (before 110 fs) and burst (after 110 fs). All the photons emitted in simulation A are considered and fixed in the emission position. In plots (a) and (b), grey lines indicate the target limits at the beginning of the simulation. The angle  $\theta$  of the distribution in (c) is zero in the laser propagation direction.

The channel dug by the laser inside the plasma has a variable diameter that follows the reduction of the laser size during propagation. Hot electrons are generated



in this channel with a broad energy spectrum reaching values up to 460 MeV. Indeed, when the interaction starts, electrons are rapidly accelerated via direct laser acceleration [60]. The trajectories of the most energetic electrons, black and blue lines in Figure 1 (b), show that, at the beginning of the interaction, the electrons are pushed backwards and then are accelerated into the channel following the laser pulse and co-moving with it. Simultaneously, the electrons experience betatron oscillations in the transverse direction driven by the magnetization of the channel, which, in addition, constrains electrons to be confined in the channel itself [60].

Some examples of the higher-energy emission are present in Figure 1 (b): the emitted photons in green by the blue electron. In general, we can distinguish two emission phases. Photons are produced firstly during laser propagation in foam; we call this *ramp phase* [43] because emission occurs at a constant rate and the energy in emitted photons grows linearly. Then, a peak of emission happens in front of the substrate (*burst phase* [43]) when electrons see the counterpropagating reflected laser field. In Figure 2 (a), the number density of all emitted photons (a) is reported. The emission occurs predominantly in the channel region of the foam, where most energetic electrons are confined. In Figure 2 (b), all the emitted photons are represented as arrows directed according to their momentum and coloured according to their energy. We can recognize low-energy backward emitted photons, especially in the early phase of interaction (left side of the channel), and higher-energy forward emission due to oscillating electrons in the channel. Most photons and the most energetic ones are emitted before the substrate during the burst phase. The distributions in Figure 2 (c) describe the directionality of photon emission in more detail. Although a background of emission is present at all angles due to the chaotic motion of electrons, photons are mainly emitted backwards during the ramp phase (blue curve) and in a cone of  $30^\circ$  around the forward direction during the burst phase (green curve). The energy distribution in the ramp phase (yellow curve) shows a more relevant contribution in energy by the forward emission due to electrons undergoing oscillations and following the laser pulse, as recognized in Figure 2 (b). During the burst phase, the emission shows two lobes peaked at  $15^\circ$ . This bilobal structure is typically observed when emitting electrons accelerated by a linearly polarized laser undergo oscillations in a near-critical plasma channel [23, 25, 27, 61, 29, 62]. The peak angle of the bilobal structure is determined by the angular deviation of betatron oscillations at the instant of copious burst emission. This angle is given by  $\phi \sim r_\beta \omega_\beta / c$  [63, 62], where  $r_\beta$  is the amplitude of the oscillations

which is approximately given by the channel radius, and  $\omega_\beta = \omega_p/\sqrt{2\gamma}$  with  $\omega_p$  the plasma frequency. Approximating  $r_\beta$  to the minimum waist achieved by the laser, i.e. 1  $\mu\text{m}$ , and  $\gamma$  to 800, which is a value achieved by the most energetic electrons in the simulation, the angular deviation of oscillations results in  $15.9^\circ$ , which is in good agreement with what we see in Figure 2 (c).

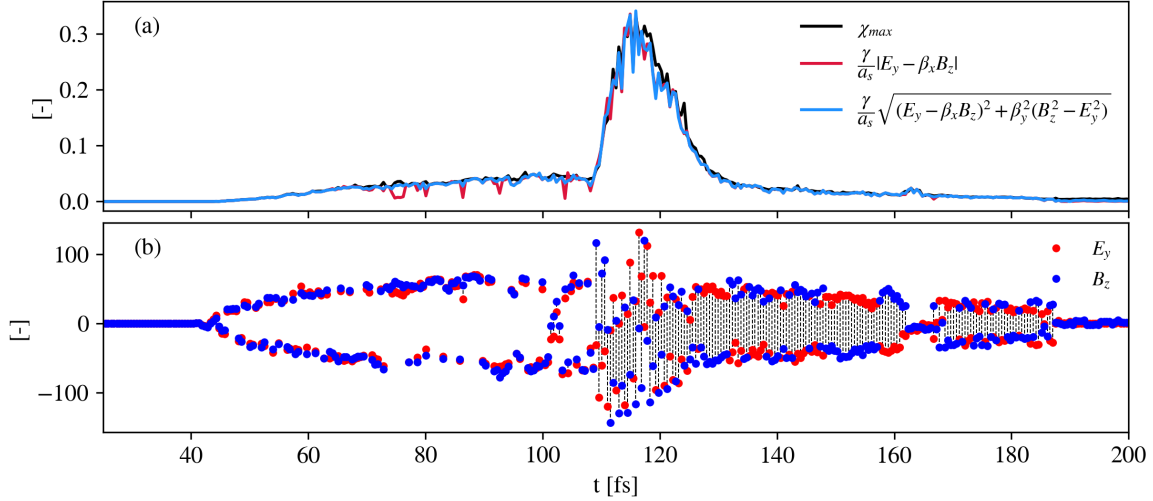


**Figure 3.** In (a), maximum values of  $\chi$  obtained during the simulation: in black, the simulation values; in red, the values computed with formula 2 considering the macroelectrons with the maximum  $\chi$ , and in blue the values calculated in the same way but with an additional correction. In (b), the electric field normalized by  $m_e\omega_0 c/e$  in the  $y$  direction (red dots) and the magnetic field normalized by  $m_e\omega_0/e$  in the  $z$  direction (blue dots) felt by the macroelectron with the maximum  $\chi$  at each timestep of the simulation diagnostic. The two field values for each macroelectron are connected with a dashed black line.

The maximum values of  $\chi$  reached by electrons are around 0.04 in the ramp phase and up to 0.33 in the burst phase. Since the electron  $\chi$  goes above 0.1 in this phase, we expect to see the impact of quantum effects [47, 3]. Using the approximation for  $\chi$  mentioned in section 1 for the counterpropagation condition, we can simply estimate the maximum value for this parameter in the burst phase using  $\chi \approx 4\pi\gamma a_f \hbar/(m_e\lambda c)$ , where  $a_f$  is the maximum normalized vector potential achieved by self-focusing. We can check that using  $\gamma \approx 800$  and  $a_f \approx 75$ , which are reasonable values for simulation A, this formula gives a  $\chi$  value around 0.33. More insights are gained by discussing a more specific approximation for  $\chi$ . Since the most relevant fields in the physical

system are the laser ones,  $E_y$  and  $B_z$ , and the electrons are mainly accelerated in the forward direction, we can evaluate  $\chi$  using this approximation of formula 1:

$$\chi = \frac{\gamma}{a_s} |E_y - \beta_x B_z| \quad (2)$$

where  $a_s = mc^2/(\hbar\omega_0)$ ,  $\beta_x = v_x/c$  with  $v_x$  the electron velocity component in laser propagation direction, and  $E_y$  and  $B_z$  are normalized by  $m_e\omega_0 c/e$  and  $m_e\omega_0/e$  respectively. As shown in Figure 3 (a) by the red line, this approximated formula describes well the maximum value of  $\chi$  achieved during the simulation. An improvement in the agreement is obtained considering also the term  $\beta_y^2(B_z^2 - E_y^2)$  due to the transversal motion of electrons (Figure 3 (a) blue line). This panel helps to understand which fields are determining the emission. Electric and magnetic fields' contributions appear with opposite signs in formula 2, meaning that if the two fields are in phase, they cancel each other, and the emission is low unless  $\beta_x$  is negative (counterpropagating electron). This case occurs in the ramp phase in which emission is mainly due to low-energy electrons travelling against the laser (see backward emission in Figure 2). Furthermore, the rising of quasi-electrostatic fields other than the laser ones and a relevant  $y$  component of electron velocity justifies further emission during the ramp phase (Figure 3 (a) blue line). In the burst phase, when reflection occurs, superposition leads to alternatively maximizing one field amplitude while lowering the other, and the  $E_y$   $B_z$  fields are phase-shifted. This effect is reported in Figure 3 (b). In the region between 110 and 130 fs,  $E_y$  and  $B_z$  values on the macroelectron with maximum  $\chi$  at each timestep (represented by connected dots) are alternatively large and small, and their signs end up being opposite. The electric and magnetic fields' contributions are not cancelling out, and  $\chi$  reaches the maximum possible values as long as hot forward-propagating electrons are available to experience these fields.

### 3.2. Comparison with analytical estimates

We compare some properties of emitted photons in simulation A with analytical results. Since Smilei simulates emission according to the LCFA and, thus, using the results for NICS in constant crossed fields, i.e. when  $\mathbf{E} \perp \mathbf{B}$  and  $|\mathbf{E}| = c|\mathbf{B}|$ , we can use the results of this theory [64, 65, 66, 67, 3] to estimate the evolution of the emitted power and the final spectrum of all emitted photons. We rearrange the formulas of this theory as functions of macro-electron properties: parameter  $\chi$ ,

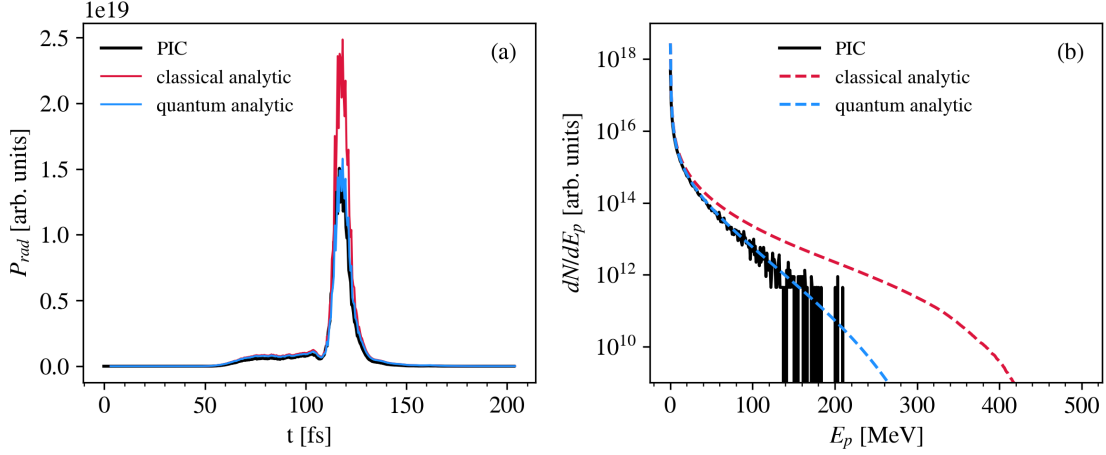


**Figure 4.** Comparison among emission properties obtained in simulation A and estimated analytically considering synchrotron emission classically or including quantum effects. Plot (a) shows the evolution in time of the emitted power densities. Plot (b) shows the final photon spectrum.

kinetic energy  $E_e$ , and numerical weight  $w_e$ . The instantaneous emitted power by all electrons is given by the summation of their contributions at a given time:

$$P_{rad} = \frac{2\alpha^2 m_e c^2}{3\tau_e} \sum_e \chi^2 g(\chi) w_e \quad (3)$$

where  $\alpha$  is the fine structure constant, and  $g(\chi)$  is equal to 1 in the classical limit and given by the following expression in the general case:

$$g(\chi) = \frac{9\sqrt{3}}{8\pi} \int_0^\infty \left[ \frac{2\xi^2}{(2+3\chi\xi)^2} K_{5/3}(\xi) + \frac{36\chi^2\xi^3}{(2+3\chi\xi)^4} K_{2/3}(\xi) \right] d\xi \quad (4)$$

where  $K_\nu$  are the modified Bessel functions of the second kind, and  $\xi$  the variable of integration. In Figure 4 (a), we have plotted the evolution of the emitted power in the simulation (black) compared with the same quantity obtained from formula 3 in the classical case (red) and with the quantum correction of formula 4 (blue). More precisely, the plotted quantities are power densities due to the reduced dimensionality of the simulations. The evolution of emitted power shows the two distinct phases we have highlighted in paragraph 3.1. The emitted power is nearly constant from 60 fs to

110 fs; thus, the energy converted in photons linearly increases: ramp phase. Instead, around 120 fs, the peak of emission characteristic of the burst phase occurs. While emission in the ramp phase is well described in a classical framework of synchrotron emission, the emission peak in front of the substrate needs quantum corrections to be estimated correctly. This fact indicates that the quantum regime of synchrotron emission is observed here. The plot confirms that the quantum effects arising when  $\chi$  approaches one reduce the emitted power against the classical case.

The energy spectrum of all emitted photons during the simulation is given analytically by a summation of electrons contributions integrated in time:

$$\frac{dN}{dE_p} = \frac{\alpha^2 m_e c^2}{\sqrt{3}\pi\tau_e} \int_{t_0}^{t_1} \sum_{E_e \geq E_p} \left\{ w_e \frac{1}{E_e^2} \left[ \frac{E_p^2}{E_e(E_e - E_p)} K_{2/3}(y) + \int_y^\infty K_{5/3}(x) dx \right] \right\} dt \quad (5)$$

where  $t_0$  and  $t_1$  are the starting and ending time of the simulation,  $E_p$  is the photon energy, and  $y$  is given by:

$$y = \frac{2E_p}{3(E_e - E_p)\chi} \quad (6)$$

Note that  $E_e$ ,  $\chi$  and, consequently,  $y$  are time-dependent quantities. The classical limit, corresponding to the usual synchrotron emission formula [53], is obtained neglecting the recoil of the radiating electrons, i.e. by taking  $E_p \ll E_e$  in equations 5 and 6:

$$\frac{dN}{dE_p} = \frac{\alpha^2 m_e c^2}{\sqrt{3}\pi\tau_e} \int_{t_0}^{t_1} dt \sum_{E_e \geq E_p} \left[ w_e \frac{1}{E_e^2} \int_y^\infty K_{5/3}(x) dx \right] \quad (7)$$

$$y = \frac{2E_p}{3E_e\chi} \quad (8)$$

In Figure 4 (b), we compare the spectrum obtained in the simulation (solid black line) with those analytically estimated in the classical case (dashed red line) and with quantum corrections (dashed blue line). The NICS spectrum is broad with an exponential shape. This shape is expected considering the typically broad, nearly exponential spectra obtained for electrons in DLTs [68, 69, 70]. The quantum corrections change the slope and cut-off of the estimated spectrum at high energy since the most energetic emission is expected to come from electrons with higher  $\chi$  and thus more affected by these corrections. The cut-off of the simulated spectrum is not present in the estimated one. This effect is due to the reduced number of particles per cell used for macro-electrons in our simulations. If this number is low,

reduced sampling affects the high-energy electrons and the photons they emit. We have tested that a visible improvement in the high-energy sampling in this plot occurs only by strongly increasing the number of macro-electrons by at least two orders of magnitude, making the simulation more expensive in computational resources.

The procedure described in this section is similar to some strategies reported in literature [71, 72] evaluating photon emission without using a Monte Carlo approach. Our estimates were performed after the simulation using the macro-electron properties saved by the diagnostics with a high time resolution. Even if the stochasticity of emission is not considered, formulas 3 and 5 can be valuable tools to check and estimate emission after PIC simulations in any case of interest and not only in the DLT case. Furthermore, this procedure can be used to recognize and evaluate the impact of quantum effects of NICS emission according to the laser and target configurations, as we have demonstrated in the DLT case.

### 3.3. Comparison with bremsstrahlung

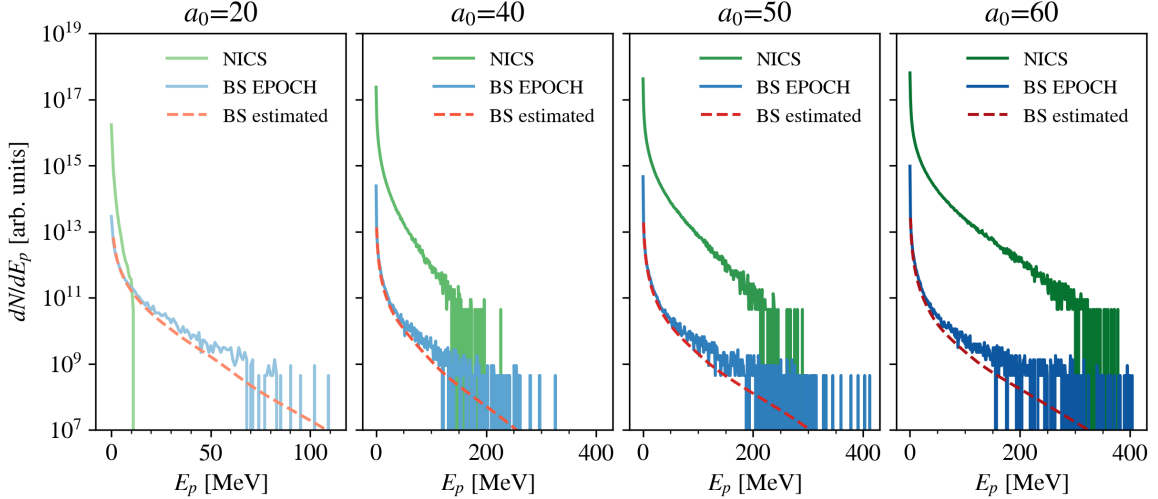


**Figure 5.** Spectra of emitted photons in the case of foam thickness 25  $\mu\text{m}$  and foam density  $1 n_c$  varying the parameter  $a_0$  (20-40-50-60). The reported spectra refer to NICS emission from SMILEI simulations (solid lines in green), bremsstrahlung (BS) emission simulated with the PIC code EPOCH (solid lines in blue) and estimated analytically (dashed lines in red).

Using analytical formulas and simulations, we can compare NICS and

bremsstrahlung in the range of parameters explored in this work. Similarly to equation 5, we can estimate bremsstrahlung generated in the substrate, which is the target region with higher density and atomic number, thus the most relevant for this type of emission. We use a generalization of the formula (7) of reference [46]:

$$\frac{dN}{dE_p} = n_i \int_{t_0}^{t_1} dt \int_{E_p}^{\infty} dE_e \left[ \frac{dN}{dE_e} v_e \frac{aZ^2}{E_p} \left( 1 - \frac{bE_p}{E_e} \right) \right] \quad (9)$$

where  $n_i$  is the ion density of the substrate,  $dN/dE_e$  is the time-dependent spectrum in energy of electrons inside the substrate,  $a=11 \cdot 10^{-31} \text{ m}^2$ , and  $b=0.83$ . In Figure 5, we report NICS-bremsstrahlung comparisons in the case of foam thickness 25  $\mu\text{m}$  and foam density 1  $n_c$  varying the parameter  $a_0$  (20-40-50-60). We show the NICS spectra obtained with Smilei (green), the bremsstrahlung spectra from analogous simulations using the PIC code EPOCH [73] that allows for Monte Carlo evaluation of bremsstrahlung [46] (blue), and the analytical estimate of bremsstrahlung using formula 9 (red). When  $a_0=40, 50, 60$ , bremsstrahlung is lower than NICS by at least two orders of magnitudes on the whole range of the spectrum. Instead, at  $a_0=20$ , NICS contribution is strongly reduced due to the relatively low laser intensity and becomes closer to bremsstrahlung contribution. In this case, the two processes contribute equally: the high-energy spectrum is dominated by bremsstrahlung, while in the low-energy portion, synchrotron radiation prevails. Overall, we deduce that the impact of NICS in our DLTs in non-extreme laser regimes is remarkably relevant. The results of Figure 5 can be discussed considering that NICS and bremsstrahlung have a different dependence on laser intensity. Bremsstrahlung depends on the electron energy achieved during the laser-driven acceleration of electrons and, thus, indirectly on laser intensity. On the other hand, NICS has an explicit dependence on intensity and the production yield goes approximately as  $a_0^3$  as demonstrated for different target cases [25, 74, 40] and approximately valid also in our parametric scan (see Figure 7 (a)). Increasing the intensity at a fixed target thickness, NICS will ultimately prevail on bremsstrahlung. Even if we are considering a foam-attached target, our results are consistent with the bare-aluminium case of [75]: in a micrometric target of aluminium, bremsstrahlung can be ignored for intensities  $> 10^{21} \text{ W/cm}^2$ . Practically, only in the case  $a_0=20$ , among those presented, NICS and bremsstrahlung are comparable. In this case, the competition between the two processes could be discussed in detail with more accurate simulations, e.g. in 3D geometry. If the thickness and/or the atomic number of the solid substrate are

changed, bremsstrahlung contribution becomes much more important [75, 17, 76] and the threshold to ignore bremsstrahlung shifts at higher intensities.

### 3.4. *Dependence on target parameters*

We report results from the whole simulation scan focusing on the dependencies of NICS emission properties on the laser and target parameters. We have chosen two properties for this analysis: the conversion efficiency from laser energy into photon energy and the average energy of all emitted photons (Figure 6). These quantities are expected to be useful in assessing the feasibility of applications and can be quantitatively evaluated in 2D simulations avoiding units altered by the reduced dimensionality. The conversion efficiencies represent the ratio between the energy in photons generated in the simulation, which have energy above  $0.25 m_e c^2$ , and the laser energy. The presence of this cut-off reduces the conversion efficiency since only the high-energy portion of the electromagnetic spectrum is considered but avoids generating a lot of low-energy photons, which can be computationally heavy to handle. Furthermore, as noted in section 3.2, low-energy emission is not affected by quantum effects and, thus, less relevant to be simulated with a Monte Carlo approach. In Figure 6 (a), we observe that the conversion efficiencies tend to show an optimum case in thickness for fixed  $a_0$  and the foam density. Exceptions are the low-density cases at high  $a_0$  where probably the scan is not covering the optimal cases corresponding to higher foam lengths, as shown by [40]. By decreasing  $a_0$  or increasing the foam density, this optimum tends to shift towards lower lengths, and its value decreases. This effect is due to the lower transparency of the plasma to the laser. Shorter foams grant that the laser can reach the reflection on the substrate and thus the counter-propagation condition of the burst phase that enhances the efficiency and energy of emission. Contrarily, the cases with dense and long foams tend to suppress the burst emission because of relevant laser absorption during the propagation, a phenomenon evidenced in [77]. Because of this, the conversion efficiencies in long foam cases increase by lowering the density. However, denser cases can become optimal at shorter foam lengths.

The average photon energy (Figure 6 (b)) shows similar optimal lengths once fixed  $a_0$  and the density. The same comments on efficiencies are valid for the average photon energy, although dense foam cases have lower performance considering this parameter even in thinner foams.



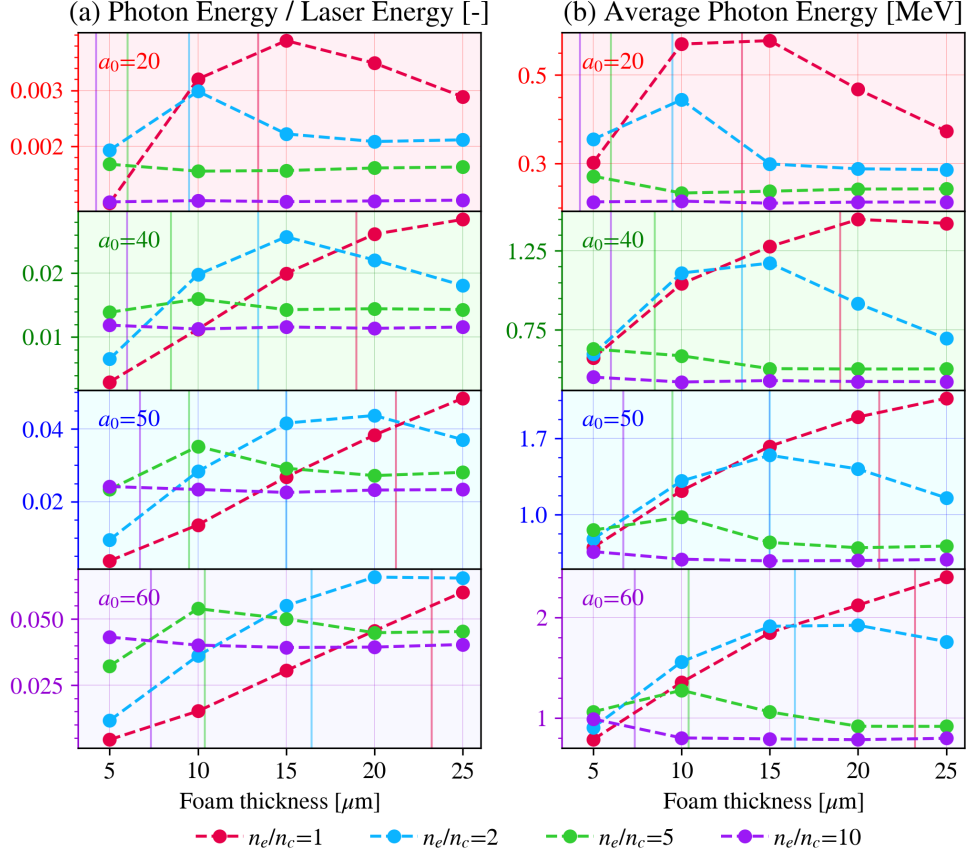


**Figure 6.** Conversion efficiency of photon energy in laser energy and average energy of all emitted photons in all the simulations performed varying  $a_0$ , foam thickness and density ( $n_e/n_c$ ). Every circle represents a simulation. Vertical lines coloured according to the density values indicate the self-focusing length.

The processes involving the laser pulse, in particular, the self-focusing and the consequent electron heating, directly impact NICS and its dependence on target parameters. 3D PIC simulations have revealed that the self-focusing effect generated by the near-critical target is representable as the action of a lens [55]. A thin-lens model can be used to obtain the focal length  $f$  of the near-critical layer and to describe the self-focusing process. This model gives  $f \approx w_0/\sqrt{\bar{n}}$  with the transparency factor  $\bar{n} = n_e/(\gamma_0 n_c)$  and  $\gamma_0 = \sqrt{1 + a_0^2/2}$ , where  $w_0$  is the beam waist

[58].  $f$  gives the rule to calculate the distance inside the foam at which the laser reaches its maximum focusing before being absorbed considerably. For example, if  $a_0 = 50$ ,  $w_0 = 3 \mu\text{m}$  and  $n_e/n_c = 2$ , the self-focusing length is equal to  $12.6 \mu\text{m}$ . Therefore, in simulation A the foam is long enough to reach the maximum possible focalization of the laser pulse. Since absorption and filamentation prevail for propagation longer than the self-focusing length, the foam thickness must be tuned to maximize the intensity when the substrate is reached, which means roughly having a foam length equal to the self-focusing length  $f$ . Despite relativistic self-focusing being an inherent 3D process, this reasoning is still valid in our 2D simulations when comparing the optimal values with the vertical lines corresponding to the self-focusing lengths in Figure 6. In many cases, the optimal length identified when fixing foam density and laser intensity is approximately the self-focusing length with a better matching when considering the average photon energy. Indeed, conversion efficiencies take advantage of laser absorption; thus, optimal values slightly longer than the self-focusing lengths are expected due to the increased laser absorption. With  $n_e/n_c=1$  at high intensities, the optimal lengths go beyond the self-focusing limit. This fact is reasonable since the transparency factor  $\bar{n}$  becomes small in these cases, and, consequently, the thin-lens model starts to fail [58].

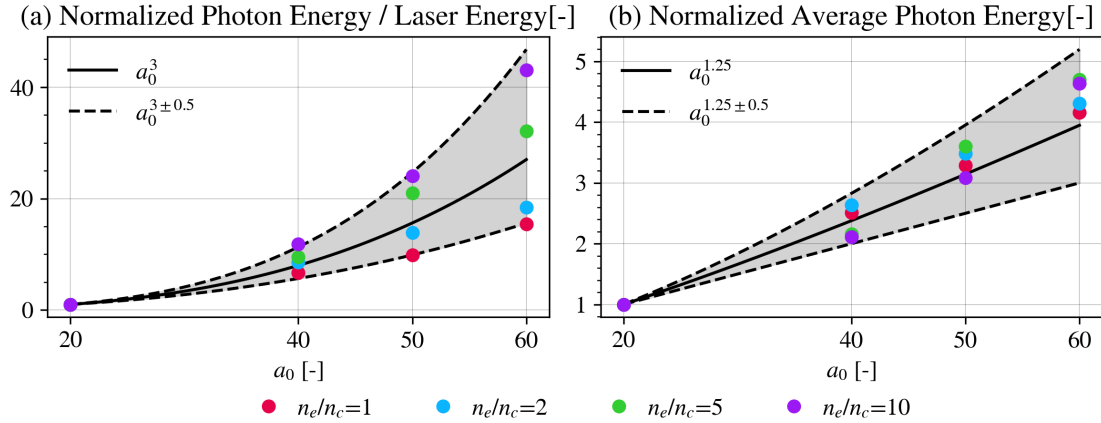


**Figure 7.** Normalized conversion efficiency of photon energy in laser energy and average energy of all emitted photons in the simulations with foam thickness closest to the self-focusing length  $f$ . Normalization is achieved by dividing by the value at  $a_0=20$  once fixed the foam density  $n_e/n_c$ . Solid and dashed black lines represent powers of  $a_0$  approximately matching the simulation point dependence.

Figure 7 reports the conversion efficiency, panel (a), and the average photon energy, panel (b), varying  $a_0$ , thus making identifiable their dependence on this parameter. The simulations considered here are only those with foam thickness closest to the self-focusing length once fixed  $a_0$  and  $n_e/n_c$ . This plot confirms a general trend reported in literature according to which the conversion efficiency from the laser in photon energy goes approximately as  $a_0^3$ . Instead, the average photon energy shows a milder dependence going approximately as  $a_0^{1.25}$ . Overall, the laser intensity proved to be the essential parameter deciding the order of magnitude of the emission properties we focused on.

Considering a nanostructured morphology for the target, the quantitative results reported in this section and the previous ones are expected to be different. We mention that, as reported in [39, 43], including a nanostructured morphology for the foam in 2D simulations has mainly the impact of reducing the photon yield and maximum photon energy due to density dis-homogeneities and more chaotic motion of electrons with respect to the uniform case, albeit remaining more efficient than the single layer. For this work, based on 2D simulations, we focus on something other than the detailed morphology expecting it to be worthy of consideration in more realistic 3D simulations. In addition, relatively high laser intensities tend to homogenize the nanostructure [78], and, if the laser contrast is not very high, the laser prepulse is expected to ionize and make the foam uniform before the interaction with the main laser peak.

#### 4. Conclusions

In this work, we have investigated NICS occurring during the interaction of an intense laser pulse ( $\sim 10^{21}$  W/cm<sup>2</sup>) with near-critical foam-based DLTs. We have focused on non-extreme laser intensities achievable in current laser facilities and on realistic target parameters. Using PIC simulations, we have recognized the main steps leading to high-energy photon emission in DLTs: laser shaping in the near-critical layer, electron heating, betatron oscillations and laser reflection on the substrate. The photon production shows two phases of emission, one related to electron motion in the self-focusing channel and the other associated with the scattering of electrons off the laser after reflection. These two phases characterize the emission in DLTs unless the laser pulse absorption in the near-critical layer prevents reflection. We have checked the simulation results against theory using analytical formulas. The

simulation gives what is expected by the theoretical scheme on which it is based. We have used these analytical formulas to evaluate the importance of using a quantum description of synchrotron radiation in the different emission phases. Emission during betatron oscillations is well-described in the classical framework, while emission in front of the substrate at laser reflection needs quantum corrections. This procedure of analytical estimates could be used to estimate NICS emission and assess the impact of quantum effects after PIC simulations in any case of interest. We have compared bremsstrahlung and NICS in some selected cases proving the impact of this second type of emission also in non-extreme regimes of laser-plasma interaction. NICS prevails on bremsstrahlung increasing the intensity, and the two phenomena seem comparable only around  $a_0=20$  with synchrotron-like emission strongly affecting the low-energy ( $<10$  MeV) portion of emitted spectra also in this case. However, if the solid substrate properties are adequately changed, bremsstrahlung contribution becomes much more relevant at higher intensities. By looking at the conversion efficiencies and average photon energies in a large simulation scan, the most promising configurations for NICS emission seem characterized by low densities ( $1-2 n_c$ ) and large foam thicknesses ( $>20 \mu\text{m}$ ) or intermediate densities ( $\sim 5n_c$ ) and short foam lengths ( $5-15 \mu\text{m}$ ). Larger values of  $a_0$  are always better to enhance the emission properties. The results show that the maximum conversion efficiencies in photon energy reached in all the simulations are around 5-6%, which is a good value considering the non-extreme intensities of this investigation. We conclude that DLTs are worth quantitative 3D numerical studies and, ultimately, experimental campaigns. On the one hand, 3D simulations could more accurately evaluate NICS and bremsstrahlung competition at relatively low intensities, quantify the brilliance of a DLT photon source, and precisely describe relativistic self-focusing assessing the relationship between optimal emission cases and the self-focusing length. On the other hand, experiments are already planned to investigate this scenario of high-energy photons production at Apollon and assess the results obtained in this work. The DLT parameters could be used to tailor emission properties making NICS dominant in experiments and exploitable in the desired applications.

## Acknowledgements

We thank Rafael Caprani for his Master Thesis [43] supervised by M.Grech, M. Passoni and A. Formenti, which set the basis of this work and was preparatory to

our analysis. We acknowledge the agreement between the Department of Energy at Politecnico di Milano and the Cineca consortium (Casalecchio di Reno, Italy) for access to the high-performance computing machines Marconi, Galileo, Galileo100 and Marconi100. This work has been carried out within the framework of the EUROfusion Consortium, funded by the European Union via the Euratom Research and Training Programme (Grant Agreement No 101052200 — EUROfusion). Views and opinions expressed are however those of the author(s) only and do not necessarily reflect those of the European Union or the European Commission. Neither the European Union nor the European Commission can be held responsible for them. The involved teams have operated within the framework of the Enabling Research Project: ENR-IFE.01.CEA “Advancing shock ignition for direct-drive inertial fusion”.

## References

- [1] Cole J, Behm K, Gerstmayr E, Blackburn T, Wood J, Baird C, Duff M, Harvey C, Ilderton A, Joglekar A, Krushelnick K, Kuschel S, Marklund M, McKenna P, Murphy C, Poder K, Ridgers C, Samarin G, Sarri G, Symes D, Thomas A, Warwick J, Zepf M, Najmudin Z and Mangles S 2018 *Physical Review X* **8** URL <https://doi.org/10.1103/physrevx.8.011020>
- [2] Poder K, Tamburini M, Sarri G, Piazza A D, Kuschel S, Baird C, Behm K, Bohlen S, Cole J, Corvan D, Duff M, Gerstmayr E, Keitel C, Krushelnick K, Mangles S, McKenna P, Murphy C, Najmudin Z, Ridgers C, Samarin G, Symes D, Thomas A, Warwick J and Zepf M 2018 *Physical Review X* **8** URL <https://doi.org/10.1103/physrevx.8.031004>
- [3] Niel F, Riconda C, Amiranoff F, Duclous R and Grech M 2018 *Physical Review E* **97** URL <https://doi.org/10.1103/physreve.97.043209>
- [4] Blackburn T G 2020 *Reviews of Modern Plasma Physics* **4** URL <https://doi.org/10.1007/s41614-020-0042-0>
- [5] Piazza A D, Müller C, Hatsagortsyan K Z and Keitel C H 2012 *Reviews of Modern Physics* **84** 1177–1228 URL <https://doi.org/10.1103/revmodphys.84.1177>
- [6] Ridgers C P, Brady C S, Duclous R, Kirk J G, Bennett K, Arber T D, Robinson A P L and Bell A R 2012 *Physical Review Letters* **108** URL <https://doi.org/10.1103/physrevlett.108.165006>
- [7] Zhang P, Bulanov S S, Seipt D, Arefiev A V and Thomas A G R 2020 *Physics of Plasmas* **27** 050601 URL <https://doi.org/10.1063/1.5144449>
- [8] Daykin T S, Sawada H, Sentoku Y, Beg F N, Chen H, McLean H S, Link A J, Patel P K and Ping Y 2018 *Physics of Plasmas* **25** 123103 URL <https://doi.org/10.1063/1.5055257>
- [9] Geddes C G, Rykovanov S, Matlis N H, Steinke S, Vay J L, Esarey E H, Ludewigt B, Nakamura K, Quiter B J, Schroeder C B, Toth C and Leemans W P 2015 *Nuclear Instruments and*

- Methods in Physics Research Section B: Beam Interactions with Materials and Atoms* **350** 116–121 URL <https://doi.org/10.1016/j.nimb.2015.01.013>
- [10] Courtois C, Edwards R, Fontaine A C L, Aedy C, Barbotin M, Bazzoli S, Biddle L, Brebion D, Bourgade J L, Drew D, Fox M, Gardner M, Gazave J, Lagrange J M, Landoas O, Dain L L, Lefebvre E, Mastrosimone D, Pichoff N, Pien G, Ramsay M, Simons A, Sircombe N, Stoeckl C and Thorp K 2011 *Physics of Plasmas* **18** 023101 URL <https://doi.org/10.1063/1.3551738>
  - [11] Ma Y, Hua J, Liu D, He Y, Zhang T, Chen J, Yang F, Ning X, Yang Z, Zhang J, Pai C H, Gu Y and Lu W 2020 *Matter and Radiation at Extremes* **5** 064401 URL <https://doi.org/10.1063/5.0016034>
  - [12] Gruse J N, Streeter M, Thornton C, Armstrong C, Baird C, Bourgeois N, Cipiccia S, Finlay O, Gregory C, Katzir Y, Lopes N, Mangles S, Najmudin Z, Neely D, Pickard L, Potter K, Rajeev P, Rusby D, Underwood C, Warnett J, Williams M, Wood J, Murphy C, Brenner C and Symes D 2020 *Nuclear Instruments and Methods in Physics Research Section A: Accelerators, Spectrometers, Detectors and Associated Equipment* **983** 164369 URL <https://doi.org/10.1016/j.nima.2020.164369>
  - [13] Habs D, Tajima T, Schreiber J, Barty C P, Fujiwara M and Thirolf P G 2009 *The European Physical Journal D* **55** 279–285 URL <https://doi.org/10.1140/epjd/e2009-00101-2>
  - [14] Mirani F, Calzolari D, Formenti A and Passoni M 2021 *Communications Physics* **4** URL <https://doi.org/10.1038/s42005-021-00685-2>
  - [15] Kmetec J D, Gordon C L, Macklin J J, Lemoff B E, Brown G S and Harris S E 1992 *Physical Review Letters* **68** 1527–1530 URL <https://doi.org/10.1103/physrevlett.68.1527>
  - [16] Gahn C, Pretzler G, Saemann A, Tsakiris G D, Witte K J, Gassmann D, Schätz T, Schramm U, Thirolf P and Habs D 1998 *Applied Physics Letters* **73** 3662–3664 URL <https://doi.org/10.1063/1.122855>
  - [17] Martinez B, d'Humières E and Gremillet L 2020 *Physical Review Research* **2** URL <https://doi.org/10.1103/physrevresearch.2.043341>
  - [18] Bulanov S S, Schroeder C B, Esarey E and Leemans W P 2013 *Physical Review A* **87** URL <https://doi.org/10.1103/physreva.87.062110>
  - [19] Bula C, McDonald K T, Prebys E J, Bamber C, Boege S, Kotseroglou T, Melissinos A C, Meyerhofer D D, Ragg W, Burke D L, Field R C, Horton-Smith G, Orian A C, Spencer J E, Walz D, Berridge S C, Bugg W M, Shmakov K and Weidemann A W 1996 *Physical Review Letters* **76** 3116–3119 URL <https://doi.org/10.1103/physrevlett.76.3116>
  - [20] Phuoc K T, Corde S, Thaury C, Malka V, Tafzi A, Goddet J P, Shah R C, Sebban S and Rousse A 2012 *Nature Photonics* **6** 308–311 URL <https://doi.org/10.1038/nphoton.2012.82>
  - [21] Esarey E, Schroeder C B and Leemans W P 2009 *Reviews of Modern Physics* **81** 1229–1285 URL <https://doi.org/10.1103/revmodphys.81.1229>
  - [22] Chen S, Powers N D, Ghebregziabher I, Maharjan C M, Liu C, Golovin G, Banerjee S, Zhang J, Cunningham N, Moorti A, Clarke S, Pozzi S and Umstadter D P 2013 *Physical Review Letters* **110** URL <https://doi.org/10.1103/physrevlett.110.155003>
  - [23] Brady C S, Ridgers C P, Arber T D and Bell A R 2013 *Plasma Physics and Controlled Fusion* **55** 124016 URL <https://doi.org/10.1088/0741-3335/55/12/124016>

- [24] Nerush E N, Kostyukov I Y, Ji L and Pukhov A 2014 *Physics of Plasmas* **21** 013109 URL <https://doi.org/10.1063/1.4863423>
- [25] Ji L L, Pukhov A, Nerush E N, Kostyukov I Y, Shen B F and Akli K U 2014 *Physics of Plasmas* **21** 023109 URL <https://doi.org/10.1063/1.4866014>
- [26] Brady C S, Ridgers C P, Arber T D and Bell A R 2014 *Physics of Plasmas* **21** 033108 URL <https://doi.org/10.1063/1.4869245>
- [27] Wang H Y, Liu B, Yan X Q and Zepf M 2015 *Physics of Plasmas* **22** 033102 URL <https://doi.org/10.1063/1.4913991>
- [28] Wu D, Qiao B and He X T 2015 *Physics of Plasmas* **22** 093108 URL <https://doi.org/10.1063/1.4930111>
- [29] Huang T W, Robinson A P L, Zhou C T, Qiao B, Liu B, Ruan S C, He X T and Norreys P A 2016 *Physical Review E* **93** URL <https://doi.org/10.1103/physreve.93.063203>
- [30] Serebryakov D A and Nerush E N 2016 *Quantum Electronics* **46** 299–304 URL <https://doi.org/10.1070/qel16051>
- [31] Chang H X, Qiao B, Zhang Y X, Xu Z, Yao W P, Zhou C T and He X T 2017 *Physics of Plasmas* **24** 043111 URL <https://doi.org/10.1063/1.4981213>
- [32] Chang H X, Qiao B, Huang T W, Xu Z, Zhou C T, Gu Y Q, Yan X Q, Zepf M and He X T 2017 *Scientific Reports* **7** URL <https://doi.org/10.1038/srep45031>
- [33] Zani A, Dellasega D, Russo V and Passoni M 2013 *Carbon* **56** 358–365 URL <https://doi.org/10.1016/j.carbon.2013.01.029>
- [34] Maffini A, Pazzaglia A, Dellasega D, Russo V and Passoni M 2019 *Physical Review Materials* **3** URL <https://doi.org/10.1103/physrevmaterials.3.083404>
- [35] Maffini A, Orecchia D, Pazzaglia A, Zavelani-Rossi M and Passoni M 2022 *Applied Surface Science* **599** 153859 URL <https://doi.org/10.1016/j.apsusc.2022.153859>
- [36] Yang Y, Jiao J, Tian C, Wu Y, Dong K, Zhou W, Gu Y and Zhao Z 2017 *Laser and Particle Beams* **35** 476–482 URL <https://doi.org/10.1017/s0263034617000490>
- [37] Gong Z, Hu R H, Lu H Y, Yu J Q, Wang D H, Fu E G, Chen C E, He X T and Yan X Q 2018 *Plasma Physics and Controlled Fusion* **60** 044004 URL <https://doi.org/10.1088/1361-6587/aaa9b1>
- [38] Gu Y J, Klimo O, Bulanov S V and Weber S 2018 *Communications Physics* **1** URL <https://doi.org/10.1038/s42005-018-0095-3>
- [39] Huang T W, Kim C M, Zhou C T, Ryu C M, Nakajima K, Ruan S C and Nam C H 2018 *Plasma Physics and Controlled Fusion* **60** 115006 URL <https://doi.org/10.1088/1361-6587/aadbeb>
- [40] Huang T W, Kim C M, Zhou C T, Cho M H, Nakajima K, Ryu C M, Ruan S C and Nam C H 2019 *New Journal of Physics* **21** 013008 URL <https://doi.org/10.1088/1367-2630/aaf8c4>
- [41] Xue K, Dou Z K, Wan F, Yu T P, Wang W M, Ren J R, Zhao Q, Zhao Y T, Xu Z F and Li J X 2020 *Matter and Radiation at Extremes* **5** 054402 URL <https://doi.org/10.1063/5.0007734>
- [42] Jirka M, Klimo O, Gu Y J and Weber S 2020 *Scientific Reports* **10** URL <https://doi.org/10.1038/s41598-020-65778-4>

- [43] Caprani R 2020 *Compact photon sources in multi-PetaWatt facilities : a kinetic numerical investigation* Master's thesis Politecnico di Milano URL <https://www.politesi.polimi.it/handle/10589/154030>
- [44] Liu J X, Ma Y Y, Yu T P, Zhao J, Yang X H, Gan L F, Zhang G B, Zhao Y, Zhang S J, Liu J J, Zhuo H B, Shao F Q and Kawata S 2016 *Plasma Physics and Controlled Fusion* **58** 125007 URL <https://doi.org/10.1088/0741-3335/58/12/125007>
- [45] Prencipe I, Metzkes-Ng J, Pazzaglia A, Bernert C, Dellasega D, Fedeli L, Formenti A, Garten M, Kluge T, Kraft S, Garcia A L, Maffini A, Obst-Huebl L, Rehwald M, Sobiella M, Zeil K, Schramm U, Cowan T E and Passoni M 2021 *New Journal of Physics* **23** 093015 URL <https://doi.org/10.1088/1367-2630/ac1fcd>
- [46] Formenti A, Galbiati M and Passoni M 2022 *Plasma Physics and Controlled Fusion* **64** 044009 URL <https://doi.org/10.1088/1361-6587/ac4fce>
- [47] Ridgers C, Kirk J, Duclos R, Blackburn T, Brady C, Bennett K, Arber T and Bell A 2014 *Journal of Computational Physics* **260** 273–285 URL <https://doi.org/10.1016/j.jcp.2013.12.007>
- [48] Gonoskov A, Bastrakov S, Efimenko E, Ilderton A, Marklund M, Meyerov I, Muraviev A, Sergeev A, Surmin I and Wallin E 2015 *Physical Review E* **92** URL <https://doi.org/10.1103/physreve.92.023305>
- [49] Lobet M, d'Humières E, Grech M, Ruyer C, Davoine X and Gremillet L 2016 *Journal of Physics: Conference Series* **688** 012058 URL <https://doi.org/10.1088/1742-6596/688/1/012058>
- [50] Blackburn T G, Seipt D, Bulanov S S and Marklund M 2018 *Physics of Plasmas* **25** 083108 URL <https://doi.org/10.1063/1.5037967>
- [51] Yoon J W, Kim Y G, Choi I W, Sung J H, Lee H W, Lee S K and Nam C H 2021 *Optica* **8** 630 URL <https://doi.org/10.1364/optica.420520>
- [52] Derouillat J, Beck A, Pérez F, Vinci T, Chiamello M, Grassi A, Flé M, Bouchard G, Plotnikov I, Aunai N, Dargent J, Riconda C and Grech M 2018 *Computer Physics Communications* **222** 351–373 URL <https://doi.org/10.1016/j.cpc.2017.09.024>
- [53] Jackson J 1998 *Classical Electrodynamics* (Wiley) ISBN 9780471309321 URL <https://books.google.it/books?id=FOBBEAAQBAJ>
- [54] Cros B, Paradkar B, Davoine X, Chancé A, Desforges F, Dobosz-Dufrénoy S, Delerue N, Ju J, Audet T, Maynard G, Lobet M, Gremillet L, Mora P, Schwindling J, Delferrière O, Bruni C, Rimbault C, Vinatier T, Piazza A D, Grech M, Riconda C, Marquès J, Beck A, Specka A, Martin P, Monot P, Normand D, Mathieu F, Audebert P and Amiranoff F 2014 *Nuclear Instruments and Methods in Physics Research Section A: Accelerators, Spectrometers, Detectors and Associated Equipment* **740** 27–33 URL <https://doi.org/10.1016/j.nima.2013.10.090>
- [55] Wang H Y, Lin C, Sheng Z M, Liu B, Zhao S, Guo Z Y, Lu Y R, He X T, Chen J E and Yan X Q 2011 *Physical Review Letters* **107** URL <https://doi.org/10.1103/physrevlett.107.265002>
- [56] Sun G Z, Ott E, Lee Y C and Guzdar P 1987 *Physics of Fluids* **30** 526 URL <https://doi.org/10.1063/1.866349>



- [57] Ren C, Duda B J, Hemker R G, Mori W B, Katsouleas T, Antonsen T M and Mora P 2001 *Physical Review E* **63** URL <https://doi.org/10.1103/physreve.63.026411>
- [58] Pazzaglia A, Fedeli L, Formenti A, Maffini A and Passoni M 2020 *Communications Physics* **3** URL <https://doi.org/10.1038/s42005-020-00400-7>
- [59] Pukhov A and ter Vehn J M 1996 *Physical Review Letters* **76** 3975–3978 URL <https://doi.org/10.1103/physrevlett.76.3975>
- [60] Arefiev A V, Khudik V N, Robinson A P L, Shvets G, Willingale L and Schollmeier M 2016 *Physics of Plasmas* **23** 056704 URL <https://doi.org/10.1063/1.4946024>
- [61] Stark D, Toncian T and Arefiev A 2016 *Physical Review Letters* **116** URL <https://doi.org/10.1103/physrevlett.116.185003>
- [62] Shen X F, Pukhov A, Günther M M and Rosmej O N 2021 *Applied Physics Letters* **118** 134102 URL <https://doi.org/10.1063/5.0042997>
- [63] Esarey E, Shadwick B A, Catravas P and Leemans W P 2002 *Phys. Rev. E* **65**(5) 056505 URL <https://link.aps.org/doi/10.1103/PhysRevE.65.056505>
- [64] Ritus V I 1985 *Journal of Soviet Laser Research* **6** 497–617 URL <https://doi.org/10.1007/bf01120220>
- [65] Baier V N, Katkov V M and Strakhovenko V M 1998 *Electromagnetic Processes at High Energies in Oriented Single Crystals* (WORLD SCIENTIFIC) URL <https://doi.org/10.1142/2216>
- [66] Sokolov A, Ternov I and Kilmister C 1986 *Radiation from Relativistic Electrons* American Institute of Physics translation series (American Inst. of Physics) ISBN 9780883185070
- [67] Berestetskii V, Lifshitz E and Pitaevskii L 1982 *Quantum Electrodynamics* Course of theoretical physics (Elsevier Science) ISBN 9780750633710
- [68] Cialfi L, Fedeli L and Passoni M 2016 *Physical Review E* **94** URL <https://doi.org/10.1103/physreve.94.053201>
- [69] Passoni M, Sgattoni A, Prencipe I, Fedeli L, Dellasega D, Cialfi L, Choi I W, Kim I J, Janulewicz K, Lee H W, Sung J H, Lee S K and Nam C H 2016 *Physical Review Accelerators and Beams* **19** URL <https://doi.org/10.1103/physrevaccelbeams.19.061301>
- [70] Passoni M, Arioli F M, Cialfi L, Dellasega D, Fedeli L, Formenti A, Giovannelli A C, Maffini A, Mirani F, Pazzaglia A, Tentori A, Vavassori D, Zavelani-Rossi M and Russo V 2019 *Plasma Physics and Controlled Fusion* **62** 014022 URL <https://doi.org/10.1088/1361-6587/ab56c9>
- [71] Martins J L, Vranic M, Grismayer T, Vieira J, Fonseca R A and Silva L O 2015 *Plasma Physics and Controlled Fusion* **58** 014035 URL <https://doi.org/10.1088/0741-3335/58/1/014035>
- [72] Niel F, Riconda C, Amiranoff F, Lobet M, Derouillat J, Pérez F, Vinci T and Grech M 2018 *Plasma Physics and Controlled Fusion* **60** 094002 URL <https://doi.org/10.1088/1361-6587/aace22>
- [73] Arber T D, Bennett K, Brady C S, Lawrence-Douglas A, Ramsay M G, Sircombe N J, Gillies P, Evans R G, Schmitz H, Bell A R and Ridgers C P 2015 *Plasma Physics and Controlled Fusion* **57** 113001 URL <https://doi.org/10.1088/0741-3335/57/11/113001>
- [74] Vyskočil J, Gelfer E and Klimo O 2020 *Plasma Physics and Controlled Fusion* **62** 064002 URL

- <https://doi.org/10.1088/1361-6587/ab83cb>
- [75] Wan F, Lv C, Jia M, Sang H and Xie B 2017 *The European Physical Journal D* **71** URL <https://doi.org/10.1140/epjd/e2017-70805-7>
- [76] Chintalwad S, Krishnamurthy S, Ramakrishna B and Ridgers C P 2022 *Physical Review E* **105** URL <https://doi.org/10.1103/physreve.105.025205>
- [77] Fedeli L, Formenti A, Bottani C E and Passoni M 2017 *The European Physical Journal D* **71** URL <https://doi.org/10.1140/epjd/e2017-80222-7>
- [78] Fedeli L, Formenti A, Cialfi L, Pazzaglia A and Passoni M 2018 *Scientific Reports* **8** URL <https://doi.org/10.1038/s41598-018-22147-6>